LA-8082

2

Response of Containment Vessels to Explosive Blast Loading

LOS ALAMOS SCIENTIFIC LABORATORY
Post Office Box 1663 Los Alamos, New Mexico 87545

An Affirmative Action/Equal Opportunity Employer

Edited by Betty Leffler.

Photocomposition by Diana Ortiz and Joni Powell.

LA-8082
UC-38
Issued: June 1980

Response of Containment Vessels to Explosive Blast Loading

Robert R. Karpp
Thomas A. Duffey*
Timothy R. Neal

*Visiting Staff Member. Department of Mechanical Engineering, University of New Mexico, Albuquerque, NM 87106.

RESPONSE OF CONTAINMENT VESSELS TO EXPLOSIVE BLAST LOADING

by

Robert R. Karpp, Thomas A. Duffey, and Timothy R. Neal

ABSTRACT

The response of steel containment vessels to the blast loading produced by the detonation of high explosives is investigated by experiments, computations, and analysis. The vessels are thin-wall shell structures that are nearly spherical. All explosive charges are solid spheres, centrally initiated and centrally positioned within the vessels. Most of the work concerns vessels that contain, in addition to the explosive charge, air at ambient or reduced pressures.

A scaling law that relates the first maximum strain occurring in the vessel wall to other relevant parameters is derived and shown to correlate the experimental data.

One-dimensional, Lagrangian, finite-difference calculations are used to study the blast phenomenon and the details of the loading pulse applied to the vessel wall. The results are verified by comparisons with pressure gauge records. In addition, vessel response to the pressure loading is calculated by both finite-difference and finite-element computer codes. The two-dimensional motion, which occurs after significant wave interactions have taken place in the test vessels, can be simulated, with reasonable accuracy, by finite-element calculations. This result indicates that a predictive technique and, therefore, a design tool appear to be available with these standard calculational methods.

The effects of a surrounding medium upon the peak strains occurring in a perfectly spherical vessel also are studied, and the reductions in strain caused by the inclusion of various surrounding media are estimated.

I. INTRODUCTION AND SUMMARY

The Los Alamos Scientific Laboratory (LASL) Dynamic Testing Division (M Division) uses a containment system capable of completely confining the products of experiments involving the detonation of high explosives. The system consists of a steel containment vessel, which is typically 1.83 m in diameter with a nominal wall thickness of 25.4 mm or 50.8 mm, mounted inside a much larger steel safety vessel. At present, LASL Group M-2 designs, monitors the fabrication and acceptance testing of, maintains, and, along with Group M-4, uses the containment and safety vessels.

In February 1977, LASL Group M-4 reinstituted its containment vessel program, which had been dormant since 1974. This report presents work accomplished under the reinstituted program, which has been designed to provide support for the explosive containment facility and to complement Group M-2's vessel program. Previous work on containment vessels, performed by both groups, has been reported informally by R. H. Warnes.[1] The present experimental work primarily involves the testing of small-scale vessels one-fifth the scale of currently used containment vessels. The pressure applied to the vessel wall and the strain in the vessel wall are measured. Most of the current testing involves the evaluation of filler materials that mitigate blast-wave effects. However, because the testing of filler materials is still in progress and definite conclusions about blast-wave mitigation have not been reached, this report summarizes the results of recent work on vessels that contain air at normal or reduced initial pressures as the filler material.

First, the one-dimensional symmetric motion of a thin spherical shell is analyzed, and the maximum strain occurring in the shell wall as a function of the loading-pulse duration is determined. For a given impulse, the maximum strain decreases rapidly when the loading duration exceeds about one-fourth of a natural one-dimensional vibration period. This fact emphasizes one obvious mechanism of blast-wave mitigation: if a filler material temporally spreads the blast wave, a decrease in the maximum strain will result.

By combining the spherical shell equation-of-motion solution with the dimensional analysis method used to develop scaling laws for blast waves, we derive a scaling law for the response of vessels to blast loading. Because the law contains the initial density of the air within the vessel as a parameter, it indicates the vessel-response sensitivity to various degrees of vacuum. If the density of the material within the vessel is held constant, this scaling law reduces to the law developed by T. R. Neal.[2] These scaling laws suggest that the amount of vessel material required to contain a specified charge depends only slightly upon the vessel radius. Within the range of tested radius-to-wall-thickness ratios ($14 \leq R/h \leq 28$), the amount of vessel material required to contain a specified explosive charge is virtually constant.

The details of the blast loading applied to the vessel wall are analyzed with the aid of one-dimensional finite-difference code calculations. Each pressure pulse has a fairly complicated structure caused by shock-wave reflections between the vessel wall and the air-explosive interface. Comparisons between pressure-gauge records and the calculations show good qualitative agreement. By using the calculated pressure pulse in conjunction with the equation describing the one-dimensional motion of a thin spherical shell, we can compute the strain history occurring in a vessel. The computed strain histories agree well with strain-gage measurements during the first half-cycle of motion. The calculated peak strain is about 20% high. The response of the test vessels after about a half-cycle of spherical motion is predominantly two-dimensional (axially symmetric). To analyze the two-dimensional response, the ADINA finite-element code is used. Comparisons between strain-gage records and finite-element calculations show good agreement. The small-scale test vessels used in this program are nearly axially symmetric with relatively large flanges around their equators. For these calculations, the strains occurring at the strain-gage locations are quite sensitive to the boundary conditions prescribed at the flanges. The flanges cause large axially symmetric perturbations in the initially spherical vessel motion. Calculations and test results show that this perturbation can cause a drastic strain amplification, which is due mostly to bending waves. Thus, a well-designed vessel should avoid this type of perturbation.

Finally, a short study of the effect of a surrounding medium on the response of spherical vessels is conducted. For the case of impulsive loading, the study compares the peak strain occurring in a vessel surrounded by a compressible fluid to the peak strain in a vessel surrounded by a vacuum.

Only the initial peak strain is considered. For water- or sand-surrounded vessels, strain reductions of about 30% or 50%, respectively, appear feasible for the geometry of interest (radius-to-wall-thickness ratio of 28). As the radius-to-wall-thickness ratio becomes larger, the beneficial effect of the surrounding medium on shell motion increases.

II. ONE-DIMENSIONAL MOTION OF A THIN SPHERICAL SHELL

Consider the spherical shell segment shown in Fig. 1. The shell thickness is denoted by h, its average radius by R, and its density by ρ. The driving pressure on the interior wall is a function of time denoted by P(t). For spherically symmetric motion, the balanced biaxial stress is denoted by σ and the radial displacement by u. Within the thin-shell approximation, the equation of motion in the radial direction is

$$\rho \frac{d^2u}{dt^2} + \frac{2\sigma}{R} = \frac{P(t)}{h} . \tag{1}$$

Hooke's law for biaxial stress is

$$\sigma = \frac{E}{1-\nu} \epsilon , \tag{2}$$

where E and ν denote Young's modulus and Poisson's ratio, respectively, and ϵ denotes the biaxial strain ($\epsilon = u/R$). A combination of Eqs. (1) and (2) produces the equation governing the one-dimensional, linearly elastic motion of a thin spherical shell. The equation is

$$\frac{d^2u}{dt^2} + \omega^2 u = \frac{P(t)}{\rho h} , \tag{3}$$

where

$$\omega^2 = \frac{2E}{\rho R^2 (1-\nu)} .$$

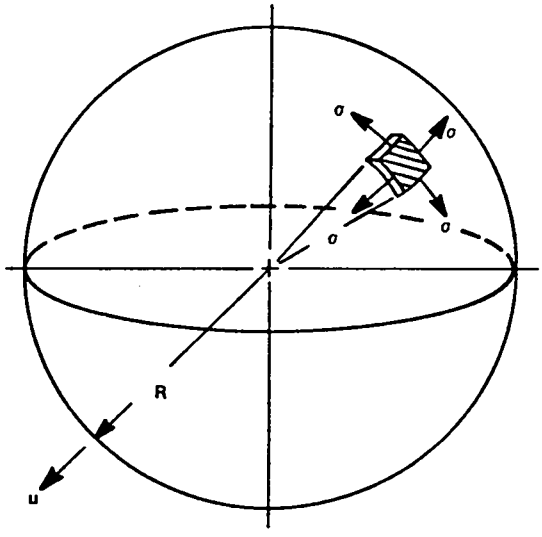

Fig. 1.
Segment of a spherical shell.

The general solution of Eq. (3) is

$$u = u_0 \cos \omega t + \frac{\dot{u}_0}{\omega} \sin \omega t + \frac{1}{\rho h \omega} \int_0^t P(\tau) \sin \omega(t - \tau) d\tau \quad , \tag{4}$$

where u_0 is the initial radial displacement and $\dot{u}_0$ is the initial radial velocity.

Consider a spherical shell acted upon by the rectangular pressure pulse illustrated in Fig. 2. The magnitude of the internal pressure pulse is p_0 and its duration is ΔT. The solutions for zero initial conditions ($u_0 = \dot{u}_0 = 0$), obtained from Eq. (4), are

$$u = \frac{P_0}{\rho h \omega^2} [1 - \cos \omega t] \text{ for } 0 \leq t \leq \Delta T \quad , \tag{5}$$

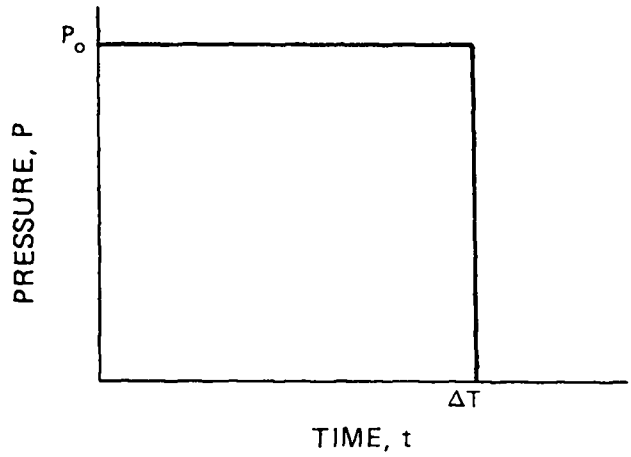

(a) RECTANGULAR PRESSURE PULSE

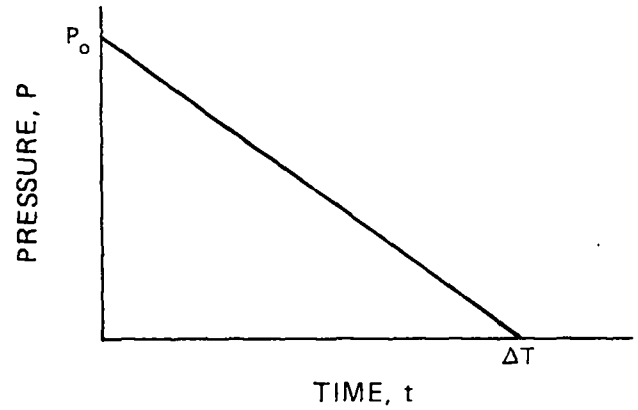

(b) TRIANGULAR PRESSURE PULSE

Fig. 2.
Pressure pulses considered in the analysis of shell motion.

and

$$u = \frac{P_o}{\rho h \omega^2} [\cos \omega(t - \Delta T) - \cos \omega t] \text{ for } t > \Delta T \tag{6}$$

The solution for a purely impulsive load, that is, a load applied over a very short time period, may be obtained from Eq. (6) by assuming that ΔT, the duration of loading, is much smaller than $T = 2\pi/\omega$, the vessel's natural vibration period. For an impulsive load, Eq. (6) reduces to

$$u = \frac{I}{\rho h \omega} \sin \omega t \quad , \tag{7}$$

where

$$I = \int_0^{\Delta T} P(t)\, dt = P_o\, \Delta T$$

is the specific impulse of the loading. From Eq. (7), the maximum strain induced by an impulsive load may be written as

$$\epsilon_{max} = \frac{I}{h\sqrt{\rho}\sqrt{\frac{2E}{1-\nu}}} \quad . \tag{8}$$

Equation (8) is true for any shaped pressure pulse as long as the loading duration is small, that is, the maximum strain is only a function of the applied impulse. However, when a pressure pulse is applied over a time period that is not small compared to T, the maximum strain induced in the shell depends upon both the pressure pulse shape and the total impulse. This feature is illustrated by again considering the motion of a spherical shell excited by the application of a rectangular pressure pulse. From Eqs. (5) and (6), the strain history may be written as

$$\epsilon(t) = \frac{I}{h\sqrt{\rho}\sqrt{\frac{2E}{1-\nu}}} f(\omega t, \omega \Delta T) \quad , \tag{9}$$

where

$$f(\omega t, \omega \Delta T) = \frac{1}{\omega \Delta T} \left[1 - \cos \omega t\right] \text{ for } 0 \leq t \leq \Delta T$$

and

$$f(\omega \Delta T) = \frac{1}{\omega \Delta T} \left[\cos \omega(t - \Delta T) - \cos \omega t\right] \text{ for } t > T \quad .$$

If $f_{max}(\omega\Delta T)$ represents the maximum value of $f(\omega t, \omega\Delta T)$ as time varies, the maximum strain can be expressed, from Eq. (9), as

$$\varepsilon_{max} = \frac{I}{h\sqrt{\rho}\sqrt{\frac{2E}{1-\nu}}} f_{max}(\omega\Delta T) \quad . \tag{10}$$

Equation (10) gives the maximum strain occurring in the shell as a function of the specific impulse, I, and the loading duration, ΔT. The form of the function $f_{max}(\omega\Delta T)$ can be determined from Eq. (9) for a rectangular pressure pulse. This function, plotted in Fig. 3, indicates the sensitivity of the peak strain in a spherical shell to the loading duration of a rectangular pulse. The maximum strain occurring in the shell decreases rapidly for loading durations greater than T/4.

The above derivation, carried out for the triangular pressure pulse shown in Fig. 2, also leads to Eq. (10) with, of course, a different expression for $f_{max}(\omega\Delta T)$. This expression is also plotted in Fig. 3. Comparing the two curves in Fig. 3 gives an idea of the sensitivity of shell response to pulse shape.

Summarizing the results, we note that the maximum circumferential strain is proportional to the applied impulse and inversely proportional to the wall thickness, the square root of the density, and the square root of twice the biaxial stress modulus, $E/(1-\nu)$, as indicated by Eq. (10). The maximum circumferential strain is also proportional to $f_{max}(\omega\Delta T)$, which accounts for the finite duration of the loading pulse. The function $f_{max}(\omega\Delta T)$ is different for pressure pulses of different shapes, and it is equal to unity for impulsive loadings. For loadings of longer duration, $f_{max}(\omega\Delta T)$ may be considerably less than unity. Thus, loadings of equal impulse may produce completely different peak strains. For a particular type of explosive charge, the loading duration depends upon both the relative size of the charge and the properties of the filler material that transmits the pressure pulse.

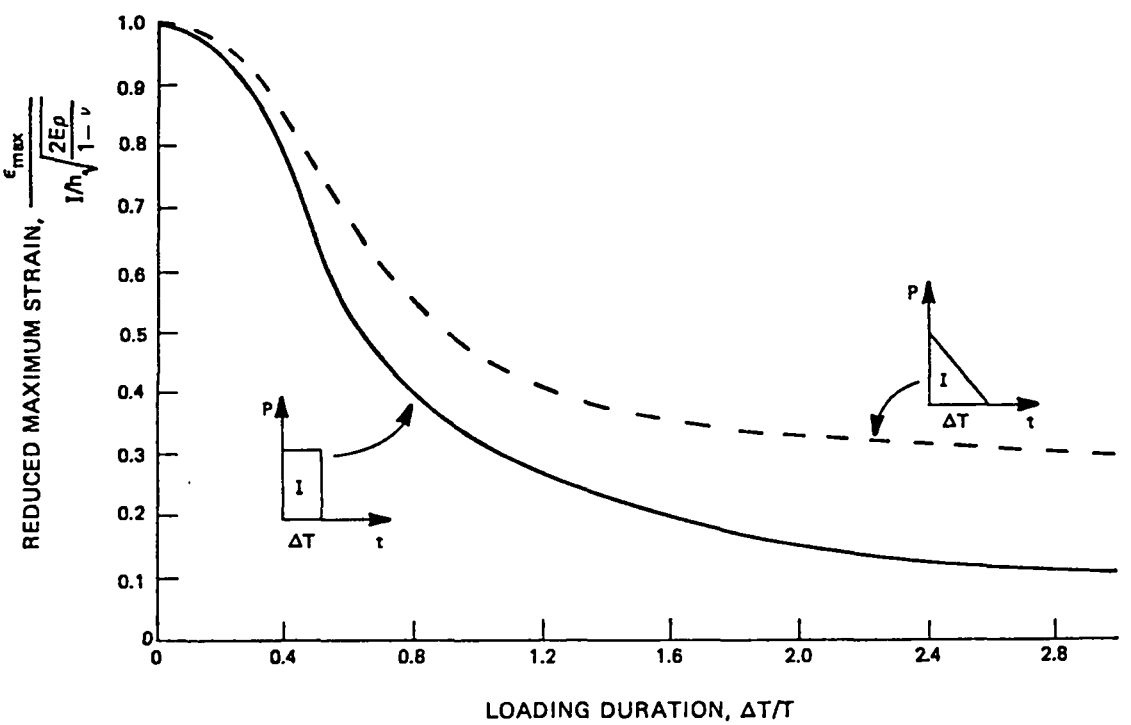

Fig. 3.
Effect of pressure pulse shape on the maximum strain of a spherical shell.

III. SCALING LAWS FOR CONTAINMENT VESSELS

Much useful information has been developed by scaling the blast-wave effects from explosive sources. For blast-wave effects in air at uniform initial conditions, the Hopkinson scaling law is used widely and is known to correlate experimental data accurately over a wide range of scaled distances.[3] To correlate blast-wave data from tests conducted with different initial conditions, for example, at different atmospheric pressures, Sach's scaling law usually is used.[3] A scaling law for vessel response can be developed by combining blast-wave scaling with equations describing the elastic motion of spherical vessels.

In this section, a scaling law for vessels is developed by assuming that the blast-wave pressure pulse applied to the vessel wall can be characterized to sufficient accuracy by two parameters, the total impulse, I, delivered to the wall and the pulse duration, ΔT. In this development, only the initial loading pulse is considered. For the analyzed configurations, subsequent loading pulses caused by wave reflections from the center of symmetry occur later in time and do not affect the vessel motion during the initial cycle. Expressions for I and ΔT are derived by following the arguments used to derive Sach's scaling law. The impulse delivered to the vessel wall is assumed to be a function of the vessel's internal radius, R_i; the energy released by detonation, W; and the properties that describe the filler material in the vessel. For the filler material, the initial density ρ_o and the initial sound speed c_o may be used to specify the state. The functional relation is $I = f_I(R_i, W, \rho_o, c_o)$. Also, we may assume that the loading duration depends upon the same set of variables; that is, $\Delta T = f_T(R_i, W, \rho_o, c_o)$. If dimensional analysis is applied to these two functional relations, they may be written as

$$\frac{IR_i^2 c_o}{W} = f_I\left(\frac{R^3 \rho_o c_o^2}{W}\right) \tag{11}$$

and

$$\frac{\Delta T c_o}{R_i} = f_T\left(\frac{R^3 \rho_o c_o^2}{W}\right) . \tag{12}$$

In Eqs. (1)—(10), which relate to the dynamics of a spherical shell, R denotes the average shell radius. In Eqs. (11) and (12), which relate to blast waves, R_i represents the vessel's internal radius. To simplify the following analysis, R_i will be approximated by the average vessel radius, R, where R is the average of the inside and outside vessel radii. This simplification introduces an additional approximation into the preceding equations describing blast waves. For thin-wall vessels, this approximation is accurate; however, for vessels with thicker walls, serious inaccuracies may result. In the present program, the test vessel with the thickest wall has an average radius-to-wall-thickness ratio of about 14. At this ratio, approximating the inside radius by the average radius introduces an error of about 4% into the radial dimension.

If Eq. (3), the expression for the vessel's natural frequency, is used with Eq. (12), an expression for the product $\omega\Delta T$ can be written as

$$\omega\Delta T = \sqrt{\frac{2E}{1-\nu}}\ \frac{1}{\sqrt{\rho}c_o}\ f_T\left(\frac{R^3 \rho_o c_o^2}{W}\right) . \tag{13}$$

Equations (11) and (13) now may be used to eliminate I and $\omega\Delta T$ from Eq. (10), the expression for the maximum strain of a spherical shell, to give

$$\varepsilon_{max} = \frac{W}{c_o R^2 h\sqrt{\rho}\sqrt{\frac{2E}{1-\nu}}} f_I\left(\frac{R^3\rho_o c_o^2}{W}\right) f_{max}\left[\sqrt{\frac{2E}{1-\nu}}\ \frac{1}{\sqrt{\rho}c_o}\ f_T\left(\frac{R^3\rho_o c_o^2}{W}\right)\right] . \tag{14}$$

Equation (14) is the general form of a scaling law for the containment of a spherical explosive charge of energy W by an elastic, spherical shell. For a specified vessel material, the constants referring to that material can be absorbed into the arbitrary functions, and the scaling law becomes

$$\varepsilon_{max} = \frac{W}{c_o R^2 h} f_I\left(\frac{R^3\rho_o c_o^2}{W}\right) f_{max}\left[\frac{1}{c_o} f_T\left(\frac{R^3\rho_o c_o^2}{W}\right)\right] . \tag{15}$$

If all tests are conducted with the same initial sound speed in the filler material, for example, air at constant initial temperature, both unknown functions depend upon the same variable and can be combined into a single unknown function. Equation (15) then can be written as

$$\varepsilon_{max}\frac{h}{\rho_o R} = f\left(\frac{R^3\rho_o}{W}\right) . \tag{16}$$

Equation (16) can be used to correlate data from tests that are conducted with different values of initial air density within the vessel. Figure 4 is a plot of data obtained from recent vessel tests. Data points inside squares represent results[2] of tests with a vessel having an internal radius of 0.889 m and a wall thickness of 63.5 mm. Data points inside circles represent the results of tests with a vessel having an internal radius of 0.176 m and a wall thickness of either 6.35 mm or 10.6 mm. All tests were conducted with the same type of high explosive (PBX-9404/9501); therefore, in the plot of Fig. 4, the explosive energy, W, was replaced by the explosive mass, M, because the

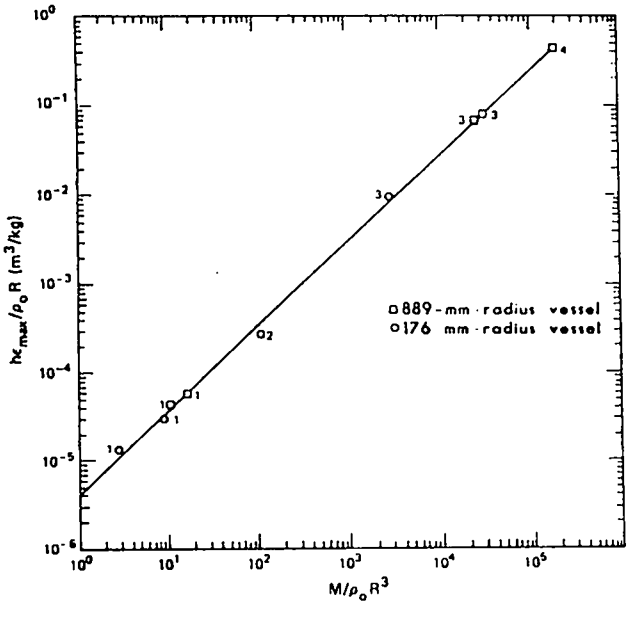

Fig. 4.
Experimental data plotted in terms of scaling law variables. Numbers adjacent to data points indicate the value of initial air density in the vessel; 1 is ρ_o = 1 kg/m³, 2 is ρ_o = 0.1 kg/m³, 3 is ρ_o = 1 × 10^{-3}, 4 is ρ_o = 5 × 10^{-5} kg/m³.

two quantities are proportional. In this test series, the initial air density within the vessel was varied. The densities used were 1.0, 0.1, 1×10^{-3}, and 5×10^{-6} kg/m^3, as indicated in Fig. 4. Strain gages mounted on the vessel walls were used to record the maximum strain. In Fig. 4, the experimental data appear to be correlated adequately by the scaling law of Eq. (16). At this point in the analysis, the applicability of the scaling law rests upon its ability to correlate the data and not upon assumptions made during its derivation. However, although the scaling law variables span a wide range of values, only the density of the filler material (air) was varied over a range of several orders of magnitude in the experiments. The remaining variables spanned a much more restrictive range.

The straight line shown in Fig. 4 is a least squares fit to the nine data points. This line has the equation

$$\frac{\epsilon_{max}\, h}{\rho_o R} = K\left(\frac{M}{\rho_o R^3}\right)^{0.961} , \tag{17}$$

where

$$K = 4.08 \times 10^{-6}\ \text{m}^3/\text{kg} .$$

This equation illustrates the slow variation of the maximum strain with a varying initial air density ($\epsilon_{max} \propto \rho_o^{0.039}$). Note that the fit given by Eq. (17) is valid only for the data range indicated in Fig. 4. As the air density in the vessel is decreased to zero, the maximum strain must approach some definite limit. Therefore, the exponent in Eq. (17) must tend toward unity as the density approaches zero.

If all tests are conducted with the same filler material at equal initial densities, Eq. (16) can be written as

$$\frac{\epsilon_{max} h}{R} = f\left(\frac{R^3}{M}\right) . \tag{18}$$

This form of scaling law has been proposed by T. Neal.[2] He has demonstrated its validity for several filler materials and has used it extensively to organize experimental results.

IV. AMOUNT OF VESSEL MATERIAL REQUIRED TO CONTAIN A SPECIFIED CHARGE

Although the minimum amount of vessel material required to contain a specific charge is not usually the governing design criterion, there may be some interest in determining this value. Equation (17) can be used to indicate how the amount of vessel material varies with the vessel radius. A combination of Eq. (17) and the expression for the volume of material in a spherical shell,

$$V_m = 4\pi R^2 h , \tag{19}$$

can be written as

$$V_m = 4\pi M \left(\frac{K}{\epsilon_{max}}\right)^{1.0406} \rho_0^{0.0406} \left(\frac{R}{h}\right)^{0.0406} . \quad (20)$$

If ϵ_{max} is interpreted as the yield point strain of the vessel material (steel) in biaxial tension, Eq. (20) specifies the volume of steel required to elastically contain the first pressure pulse from a mass, M, of PBX-9404/9501 explosive. Figure 5 shows the volume of vessel material as a function of the radius-to-thickness ratio of the vessel for the special case of an 8.16-kg (18-lb) explosive charge with $\epsilon_{max} = 0.0011$ and $\rho_o = 1.0$ kg/m³. Figure 5 indicates the very slow variation in the amount of vessel material required to contain the dynamic load generated by the explosive as the radius-to-thickness ratio, R/h, is varied. The variation in material volume over the experimental range of $14 \leq R/h \leq 28$ is only about 3%. The total range plotted in Fig. 5 shows only 7% variation in material volume. Thus, the amount of material required to contain a specified charge in this range of configurations is essentially constant. However, very thin wall, large-radius vessels would make inefficient use of material, at least for blast-wave containment.

The above analysis applies only to the containment of the initial pressure pulse. The effect of subsequent pressure pulses is best treated by numerical calculations and is presented in Sec. VI. However, for long-term containment, the strain caused by the final static pressure also needs to be estimated. The static pressure can be estimated from the semiempirical formula[4]

$$P_s = C \frac{M}{V} , \quad (21)$$

where V is the internal volume of the vessel and C is a constant with a value of about 1.3 m³ MPa/kg for most solid explosives. The volume of vessel material required to contain the static pressure elastically can be estimated from Eq. (21) for the specific case illustrated in Fig. 5. This material volume, also plotted in Fig. 5, is independent of the radius-to-thickness ratio if the internal radius is approximated by the average radius of the vessel and the usual formula for equilibrium of a thin shell is used. The material volume required to contain the static load is only about 15% of that required to contain the initial dynamic load.

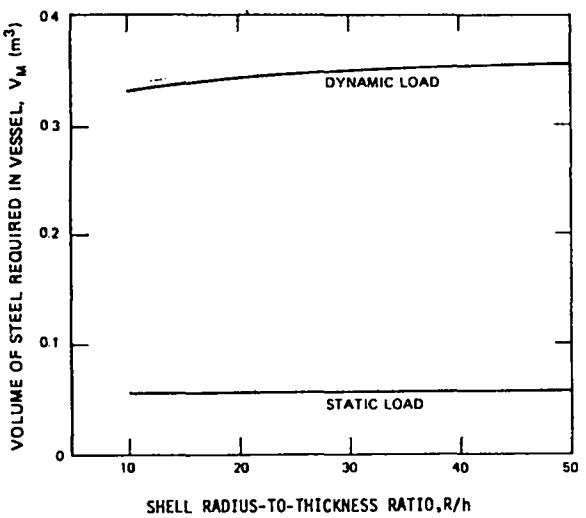

Fig. 5.
Volume of vessel material required to contain 8.16 kg of PBX-9404 as a function of vessel radius-to-thickness ratio for a steel vessel ($\epsilon_{yield} = 0.0011$, $\rho_o = 1$ kg/m³).

V. PRESSURE LOADING ON VESSEL WALLS

A. Calculation of Pressure Loading

To qualitatively understand the pressure loading on the vessel wall and to establish a predictive capability, computer hydrodynamic calculations of the motion of the explosive and filler material within the containment vessel were performed. In the calculations, spherical symmetry was assumed. The computer code used to perform them is based on a fairly common one-dimensional, Lagrangian, finite-difference technique similar to the one described by Fickett.[5] Initially, the explosive is assumed to be burned completely, and the distribution of properties within the explosive products is determined from the Taylor similarity solution.[6] In these calculations, the equation of state used to describe the explosive products is the JWL equation.[7] The filler material considered here is either air or a perfect vacuum. For air, a γ-law equation of state was used with $\gamma = 1.4$. The shell velocity is obtained by numerically integrating Eq. (3) along with the numerical solution of the hydrodynamic equations. The results of a calculation involving

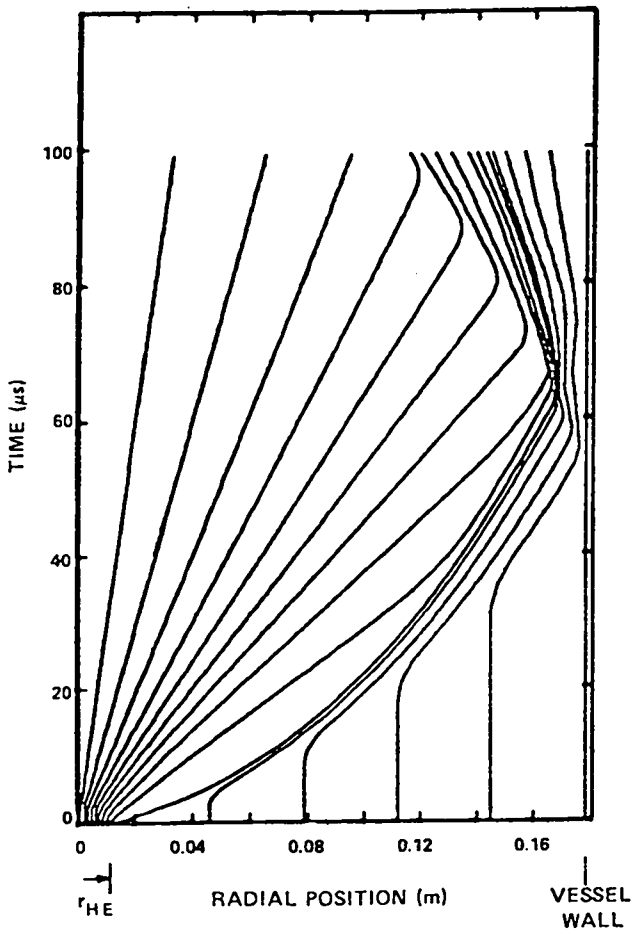

Fig. 6a.
Plot of numerically calculated particle paths [25.4-mm-diam spherical explosive charge (HE) of mostly PBX-9404 in a 0.352-m-diam vessel filled with air at 79 kPa (0.78 atm) pressure].

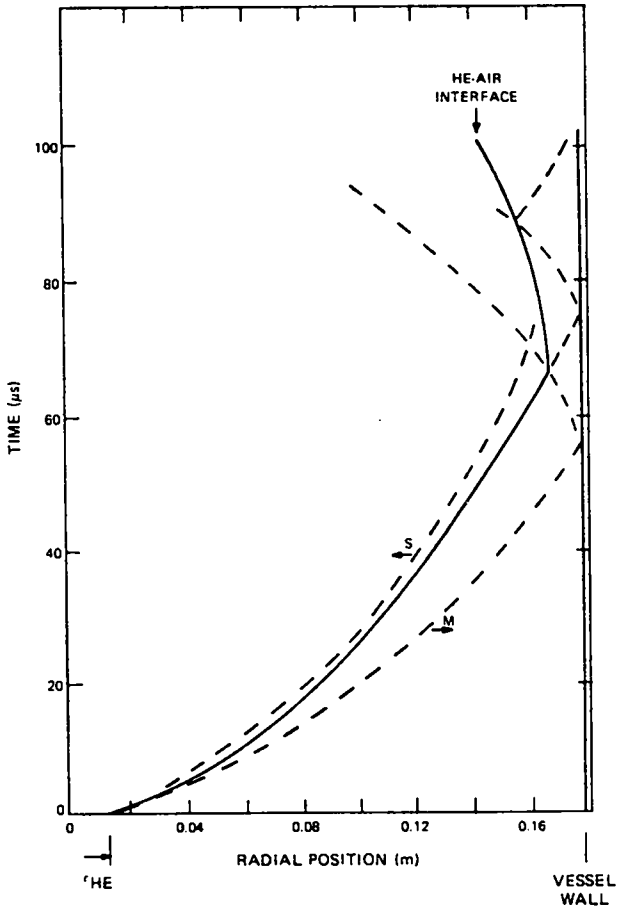

Fig. 6b.
Location of some of the shock waves occurring in the flow of Figure 6a.

a 25.4-mm-diam explosive charge of PBX-9404 in an air-filled, 352-mm-diam vessel are illustrated in Fig. 6a. This figure is a plot of the position of several particles within the flow field as a function of time; it gives an idea of the wave motion set up within the vessel. Figure 6b, obtained from Fig. 6a, indicates some of this wave motion. Shock wave positions are indicated by dotted lines. The main shock, M, is followed by a secondary shock, S, which propagates inward relative to the moving explosive products. The secondary shock, formed because of the spherically diverging flow discussed by Brode,[5] produces a high-density region between the secondary shock and the air-explosive interface. This condition is illustrated in Fig. 7, where the pressure and density distributions are shown at 40 μs, shortly before the main shock reaches the vessel wall.

The main shock front reflects from the vessel wall at 53 μs and collides with the air-explosive interface at 63 μs, as indicated in Fig. 6b. At that point, part of the wave is transmitted into the explosive products, but, because of the high-density region, another, substantial part is reflected into the air. The reflected part impinges on the vessel wall at 70 μs. Therefore, we would expect to

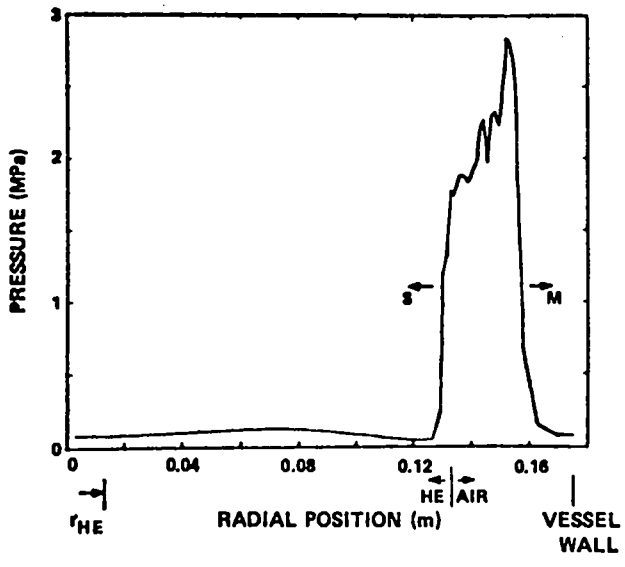

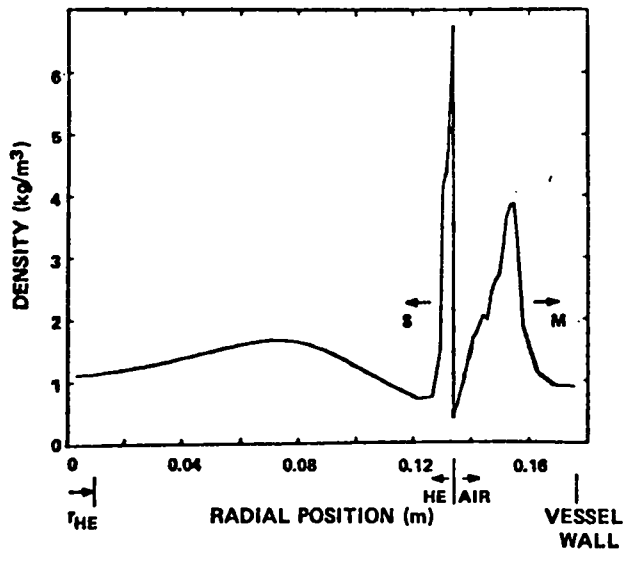

Fig. 7.
Pressure and density distributions at 40 μs after explosive detonation (configuration indicated in Fig. 6a).

see a second loading pulse applied to the vessel wall at this time. Figure 8 shows the calculated pressure pulse applied to the vessel wall for the first 200 μs. Here the initial pressure loading at 53 μs and the second pressure loading at 70 μs are apparent. The shock wave that causes the second loading continues to rebound between the interface and the vessel wall, but additional pressure pulses caused by its subsequent reflections are of negligible amplitude for this example.

The pressure on the vessel wall continues to drop until the main shock front is reflected from the center of symmetry and propagates out to the vessel wall. The reflected wave arrives at the vessel wall at 240 μs and produces the second major loading pulse. Figure 9 shows the arrival of the second major loading pulse as well as several subsequent major loading pulses. A double-peaked structure caused by a wave reflection from the air-explosive interface is apparent within each major loading pulse.

A change in the relative size of the explosive charge changes the shape of the pressure pulse applied to the vessel wall. The pressure pulse illustrated in Fig. 8 was generated by an explosive charge whose radius was 7% of the vessel radius. Figure 10 shows how the shape of the first major loading pulse changes as the size of the explosive charge changes. With a charge that is 14% of the

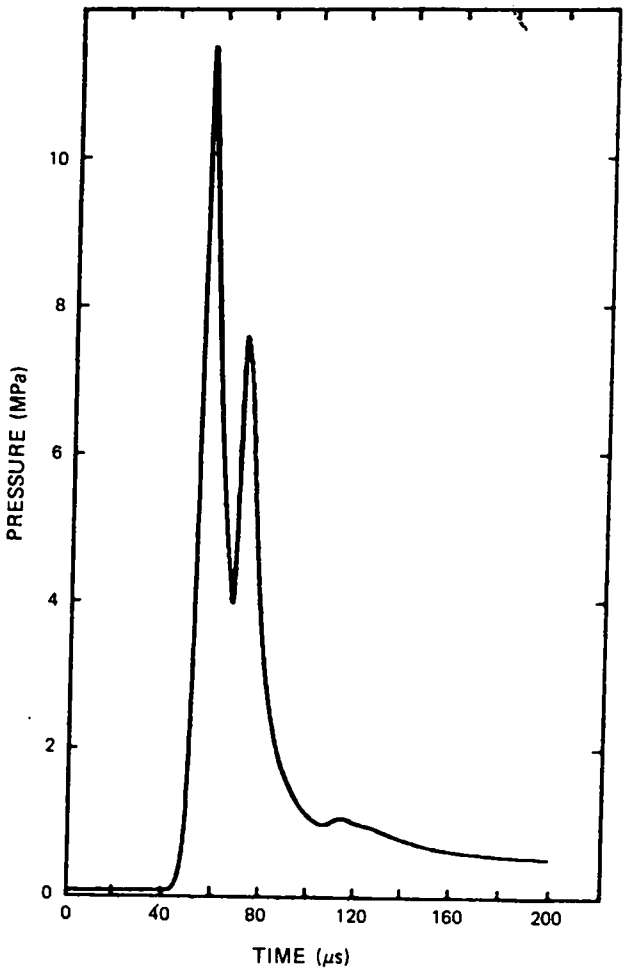

Fig. 8.
Calculated pressure pulse acting on the vessel wall (0-200 μs, configuration indicated in Fig. 6a).

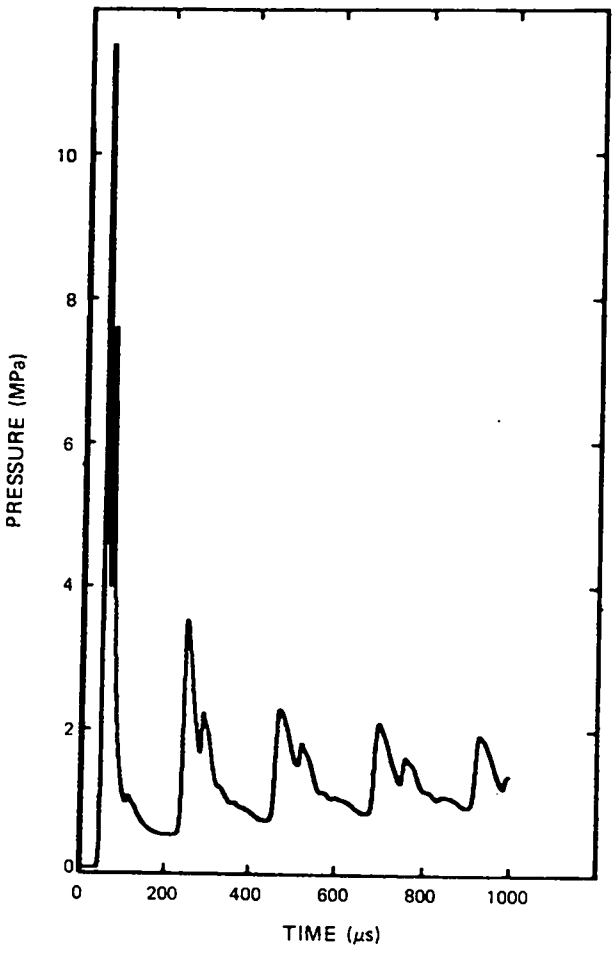

Fig. 9.
Calculated pressure pulse acting on the vessel wall (0-1000 μs, configuration indicated in Fig. 6a).

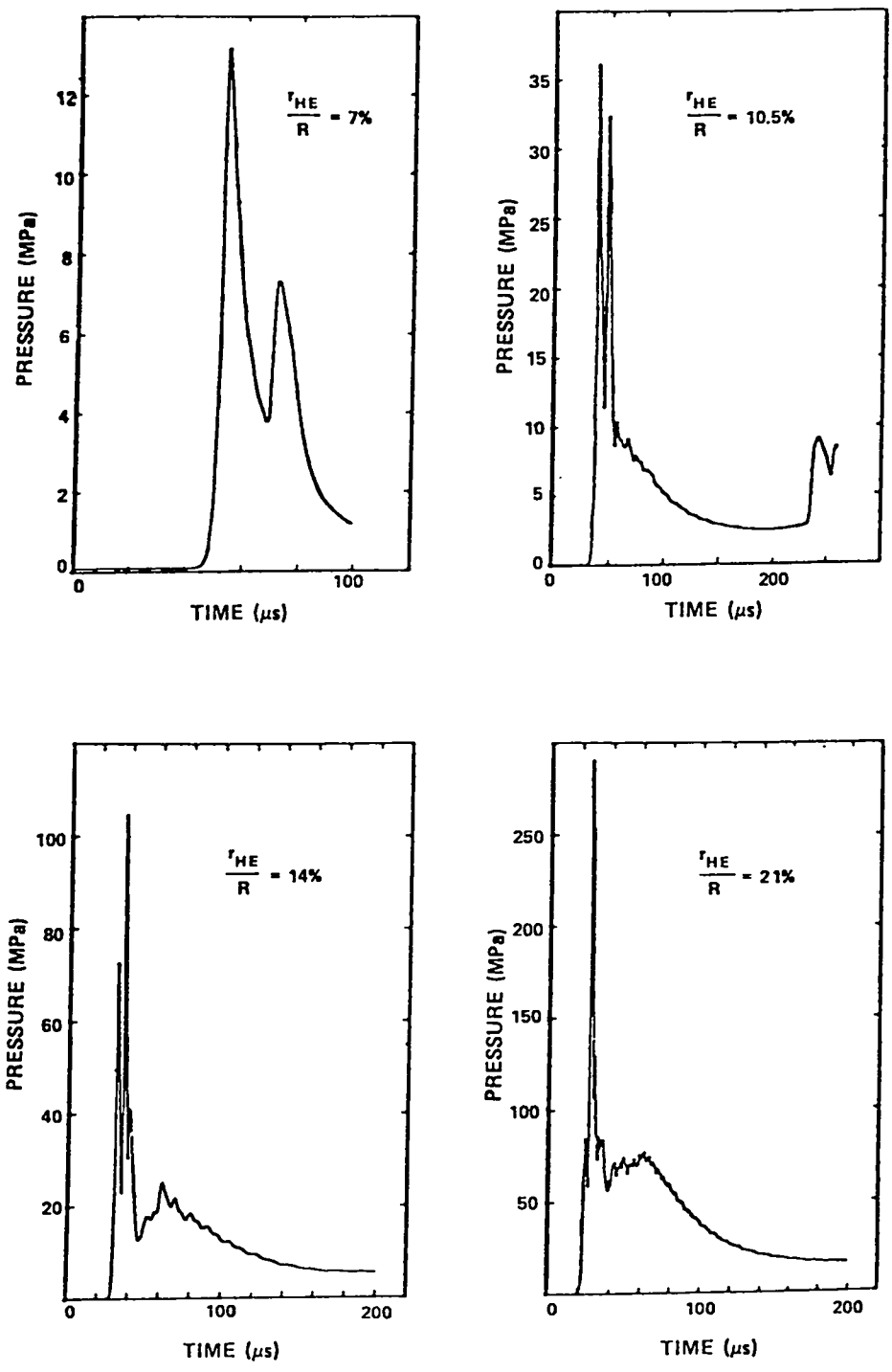

Fig. 10.
Calculated pressure pulses for various size explosive charges.

vessel radius, the second pressure pulse, caused by the reflected wave, is larger than the initial pressure pulse, caused by the arrival of the main shock front.

B. Comparisons of Measured and Computed Pressure Histories

Comparisons between measured and numerically calculated pressure pulses are illustrated in Figs. 11, 12, and 13. For the two tests conducted with the vessel containing air at normal density, Figs. 11 and 12, a good qualitative agreement is indicated between measurements and calculations. However, the calculated pressures appear to be quantitatively higher than the measurements. For the calculation of an evacuated vessel, Fig. 13, complete air evacuation was assumed. For this experiment, however, an initial air pressure of about 100 Pa existed in the vessel. The calculations indicate that a high-pressure spike arrives at the vessel wall before the main pressure pulse. This pressure spike is quite high in magnitude but short in duration and may be an artificial result of the numerical method. The experimental records show some high-frequency, high-pressure pulses; these are attributed to an air shock, since the vessel is not completely evacuated. Because the pressure-gauge response is not sufficient to resolve this high-frequency behavior at the beginning of the pressure pulse, the initial high-frequency data have been ignored in the measured pressure pulse of Fig. 13. Aside from the very early data, which may not be significant with respect to the vessel response, a good qualitative and quantitative agreement exists between measurements and calculations.

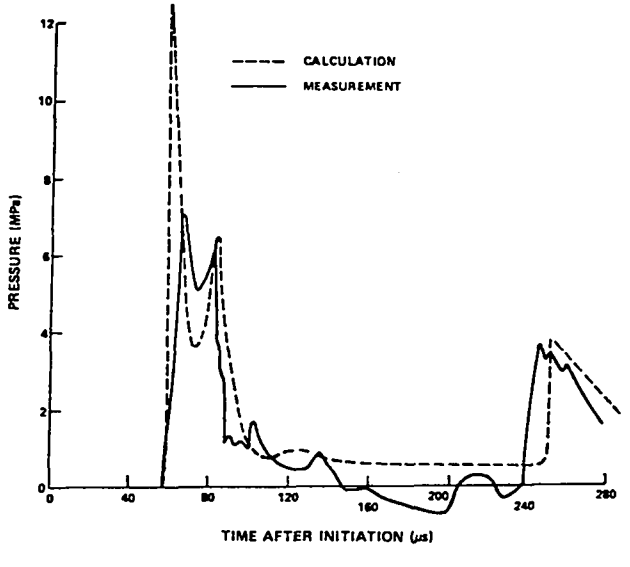

Fig. 11.
Comparison of measured and calculated pressure acting on the vessel wall (parameters indicated in Fig. 6a).

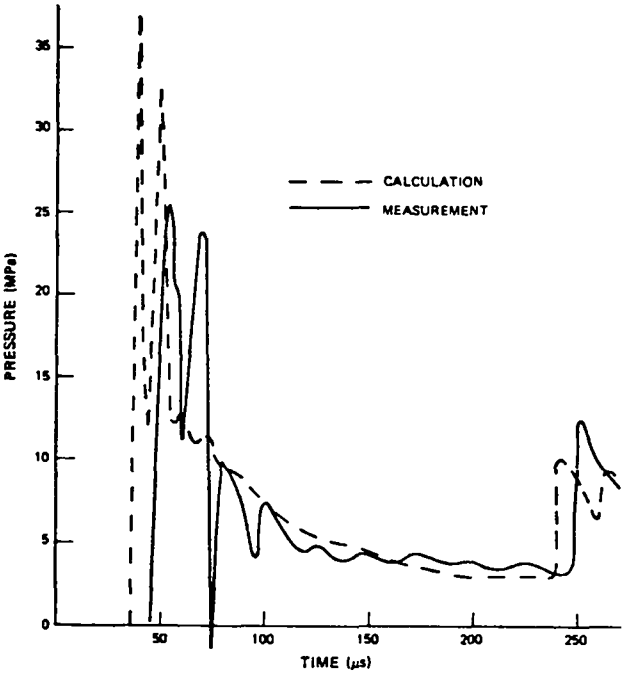

Fig. 12.
Comparison of measured and calculated pressure acting on the vessel wall (38.1-mm-diam explosive charge, other parameters indicated in Fig. 6a).

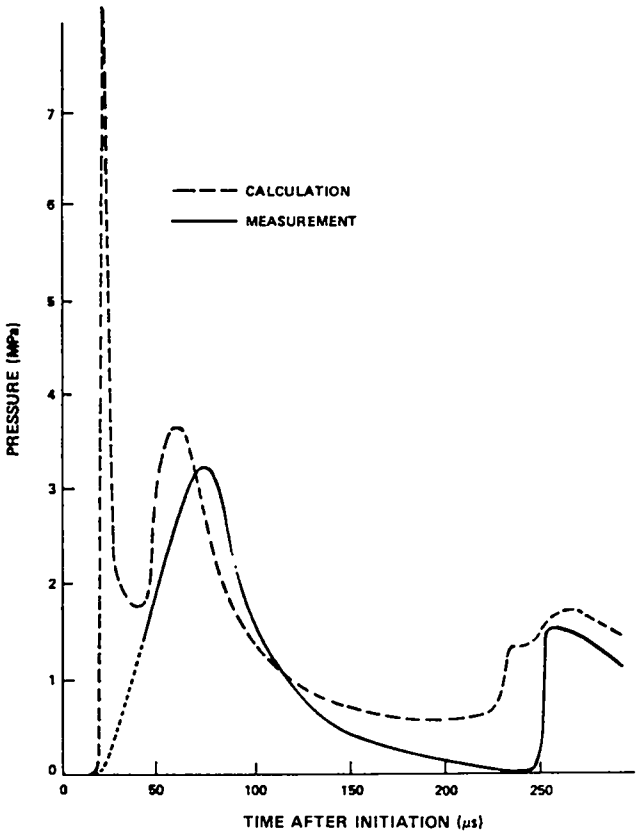

Fig. 13.
Comparison of measured and calculated pressure acting on the vessel wall (ρ_o = 1 g/m³ vacuum case, other parameters indicated in Fig. 6a).

VI. RESPONSE OF VESSELS TO BLAST LOADING

A. One-Dimensional Vessel Response

The equation of motion of a thin spherical shell, Eq. (3), can be solved for any pressure loading by numerical integration. Figure 14 shows the resulting strain history obtained by integrating Eq. (3) for the pressure loading illustrated in Figs. 8 and 9. The first major loading pulse lasts about 50 μs and initiates the sinusoidal motion of the vessel wall. If no other pressure pulses were applied to the wall, the vessel would continue to oscillate at constant amplitude in the one-dimensional case. However, the second major pressure pulse arrives at the vessel wall at about 220 μs, when the vessel wall has expanded but is moving inward. Therefore, the second major pressure pulse opposes the motion of the vessel wall and reduces the oscillation amplitude. For the calculation illustrated in Fig. 14, the decrease in the oscillation amplitude caused by the arrival of the second pressure pulse is approximately 40%. Subsequent pressure pulses increase the oscillation amplitude again; the amplitude at 1 ms is about 75% of the initial value. Figure 14 indicates the relative importance of the various pressure pulses that dynamically load the vessel wall. From these calculations, we find that the second major loading pulse causes a reduction in the oscillation amplitude for PBX-9404 charges whose radii are between 7% and 14% of the vessel radius. Other cases have not been explored.

Figure 15 shows a small-scale test vessel used to measure pressure and strain. Tests recently have been conducted with two slightly different vessels, the thin-wall vessel (6.35-mm wall) illustrated in Fig. 15 and a thick-wall vessel (10.6-mm wall). The thick-wall vessel is similar in design to the thin-wall vessel, but the flanges are considerably larger. Both vessels vibrate

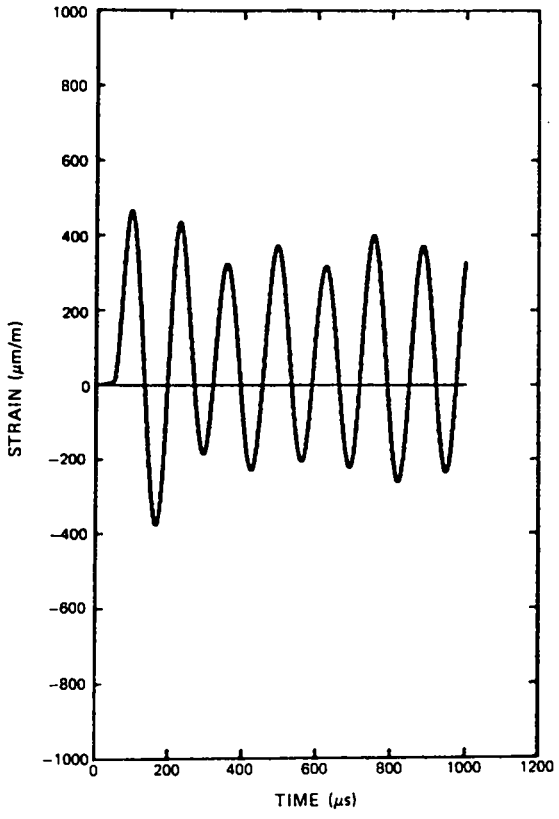

Fig. 14.
Calculated strain based upon the one-dimensional shell theory (steel vessel with a 6.35-mm-thick wall, pressure loading shown in Figs. 8 and 9).

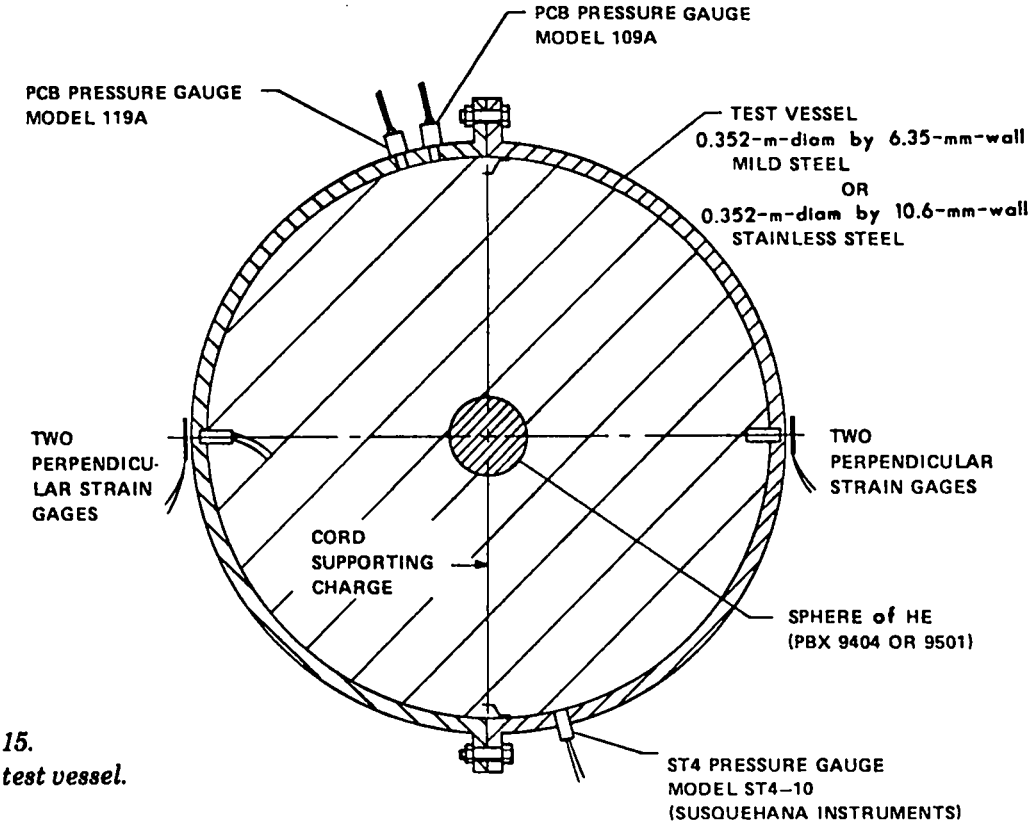

Fig. 15.
Small-scale test vessel.

primarily in a two-dimensional mode. When the inside of the vessel wall is loaded by a spherically symmetric pressure pulse, the wall motion in the strain-gage area will be one-dimensional until a disturbance arrives from the flanges. From that time, the motion will be mainly two-dimensional. It takes about one-half period of the vessel's natural vibration for a wave to propagate from the flange area to the strain-gage area, so we would expect to observe a true one-dimensional motion at the strain gages for about the first half-cycle of vibration. For these test vessels, a valid comparison between calculated strains based on the assumption of spherically symmetric motion and measured strains can be made only for the first 60 μs of motion.

Figures 16, 17, and 18 compare the calculated and measured strain histories. Figure 16 shows the response of the thin-wall vessel to the detonation of a 25.4-mm-diam PBX-9404 charge when the vessel is filled with air at normal conditions. Comparing only the first strain pulse because the following motion will be perturbed by two-dimensional effects, we see that the calculated first peak strain is about 20% higher than the average of the four strain-gage measurements. However, the calculated value agrees quite well with strain-gage measurements 1 and 4. Figure 17 shows the response of the thick-wall vessel to the detonation of a 38.1-mm-diam PBX-9404/9501 charge when the vessel is filled with air at normal conditions. Again comparing only the first strain pulse, we see that the calculated peak is about 40% higher than the average of the strain-gage records, although the calculated value agrees quite well with gage records 3 and 4. Figure 18 shows the calculated and measured strains resulting from the detonation of a 25.4-mm-diam charge in a vessel that has been evacuated to about 100 Pa. The agreement between calculated and measured first peak strains is about 5% for all gages. In this test, the first peak strain was not indicated clearly by gage record number 1.

Generally, these calculations give reasonable estimates of the first peak strain amplitude. Even better estimates of the pressure loading and, therefore, better quantitative agreement between measured and calculated peak strains might be obtained by using calculations based upon extensively calibrated equations of state for both the explosive products and the air.

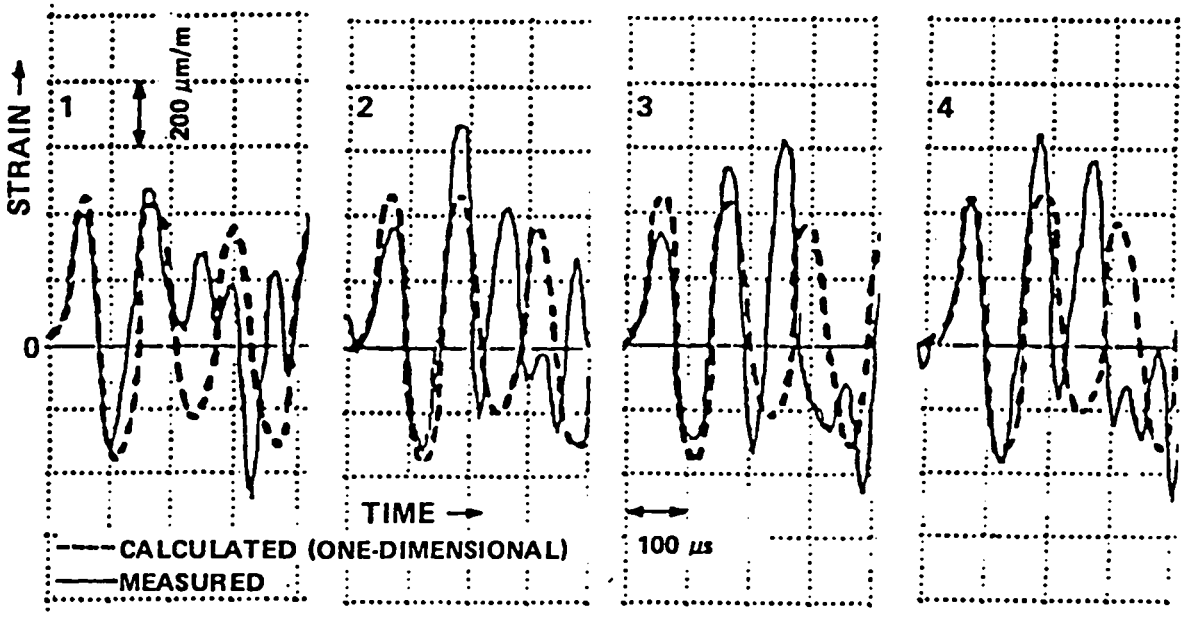

Fig. 16.
Comparison of measured and calculated vessel strain, with the calculation based upon one-dimensional motion (0.352-m-diam vessel with a 6.35-mm-thick wall, 25.4-mm-diam PBX-9404 charge, air filled).

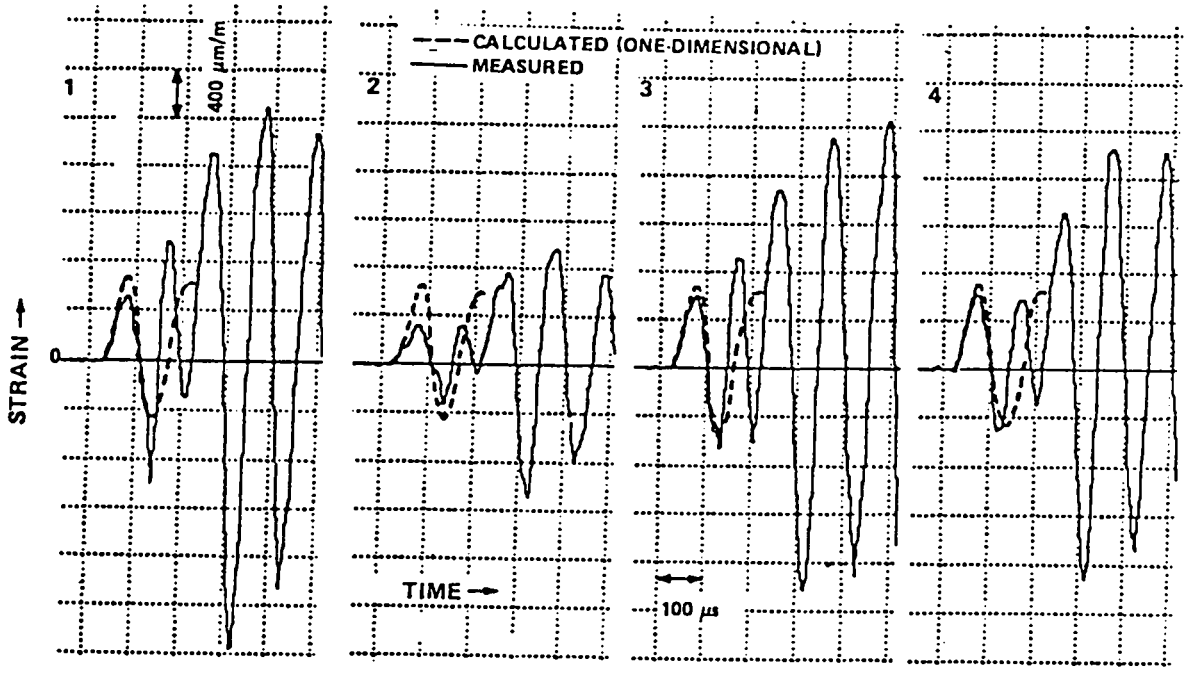

Fig. 17.
Comparison of measured and calculated vessel strain, with the calculation based upon one-dimensional motion (0.352-m-diam vessel with a 10.6-mm-thick wall, 38.1-mm-diam charge, air filled).

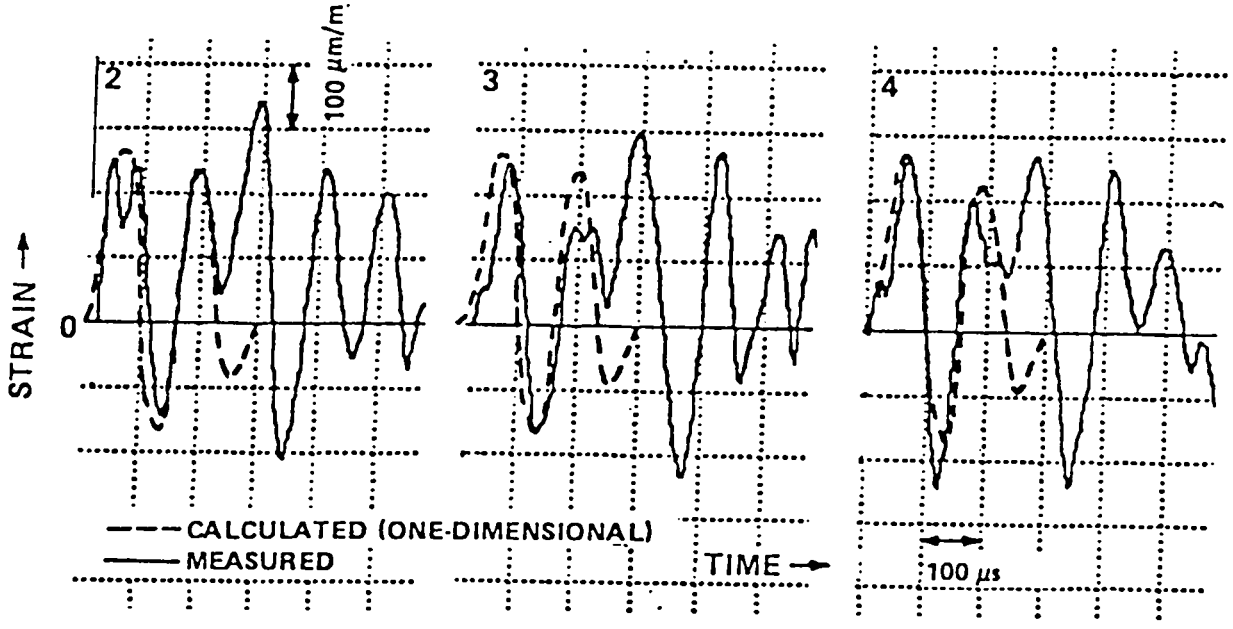

Fig. 18.
Comparison of measured and calculated vessel strain, with the calculation based upon one-dimensional motion (0.352-m-diam vessel with a 6.35-mm-thick wall, 25.4-mm-diam charge, vacuum).

B. Two-Dimensional Vessel Response

As indicated above, the motion of these test vessels is primarily two-dimensional (axially symmetric) because of the relatively large flanges, which induce significant axially symmetric perturbations to the spherical motion. Waves originating in the flange area converge at the spherical shell's poles, where the strain gages are mounted. The convergence increases the strain amplitude at the strain-gage location from two (thin-wall vessel) to five (thick-wall vessel) times the initial strain amplitude. This amplitude increase can be seen in the strain records of Figs. 16 and 17.

To predict this fairly complicated motion, a two-dimensional analysis is required. Given the proper loading conditions, finite-element codes should be able to adequately simulate vessel response. By comparing these gage data with computational results we can assess the applicability of finite-element codes to dynamic pressure vessel design problems. The ADINA[9] finite-element code was chosen for this analysis because of its availability. Figure 19 shows the finite-element models, in the cylindrical coordinates R and Z, that were used to represent both thin-wall and thick-wall vessels. In the calculations, the shell structure of the vessel was

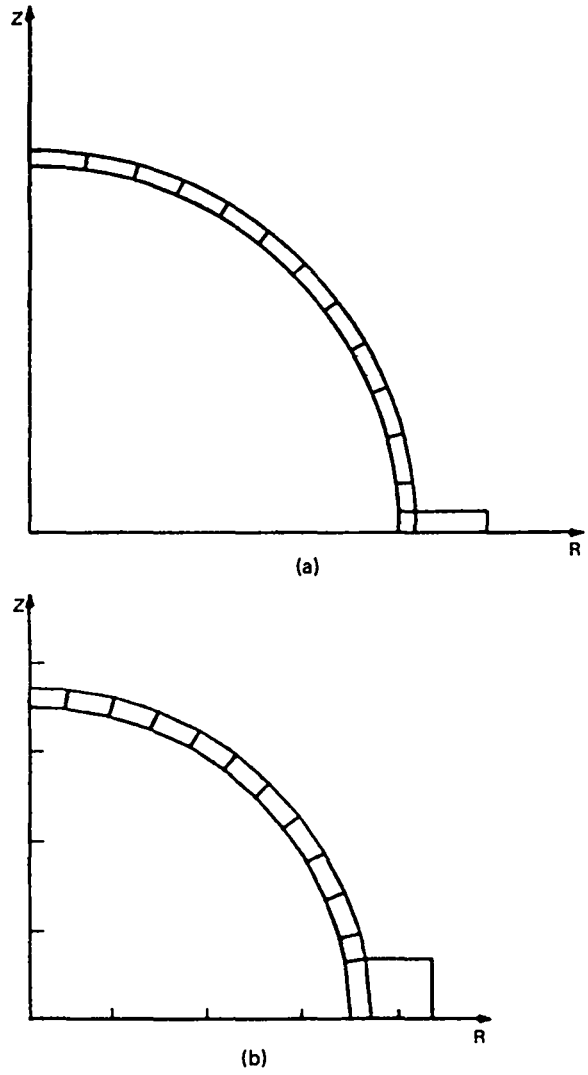

Fig. 19.
Finite-element models used in the ADINA code to calculate the response of (a) the thin-wall test vessel and (b) the thick-wall test vessel.

represented by only one element across its thickness. The type of element used was the eight-node, axially symmetric element. A minimum number of elements was used to represent this vessel in the two-dimensional analysis because interest eventually will lie in analyzing three-dimensional vessels and extension to the three-dimensional problem then will not lead to decreased resolution.

Figure 20 shows the results of two ADINA code calculations for the motion of the thin-wall test vessel subjected to the internal pressure loading illustrated in Figs. 8 and 9 (a 25.4-mm-diam explosive charge in an air-filled vessel). The results are the values of circumferential strain occurring at the center of the outside surface of the element near the hemisphere pole, where the strain gages are bonded to the vessel. In the fixed-flange calculation, we assumed that the flange bottom remained in contact with the symmetry plane (z = o); see Fig. 19. In the free-flange calculation, we assumed that the flange was free to move off the axis of symmetry. Because the flanges are held together by 24 equally spaced bolts, the true boundary condition to which the flange is subjected lies somewhere between these two extremes. From the results shown in Fig. 20, we can conclude that the strain history at the vessel poles is a strong function of the boundary conditions applied to the flanges. This sensitivity has been indicated by App and Snell.[10]

Figure 21 shows a comparison between the free-flange calculation of Fig. 20 and a strain-gage measurement. The agreement is fairly good, especially if we consider that a calculated pressure loading was used as input and that a very coarse zoning was used. Notice that the strain-gage measurement is saturated at about 550 μs, about the time when the calculated strain reaches its absolute maximum. A linear elastic analysis was used in ADINA because the strain amplitude

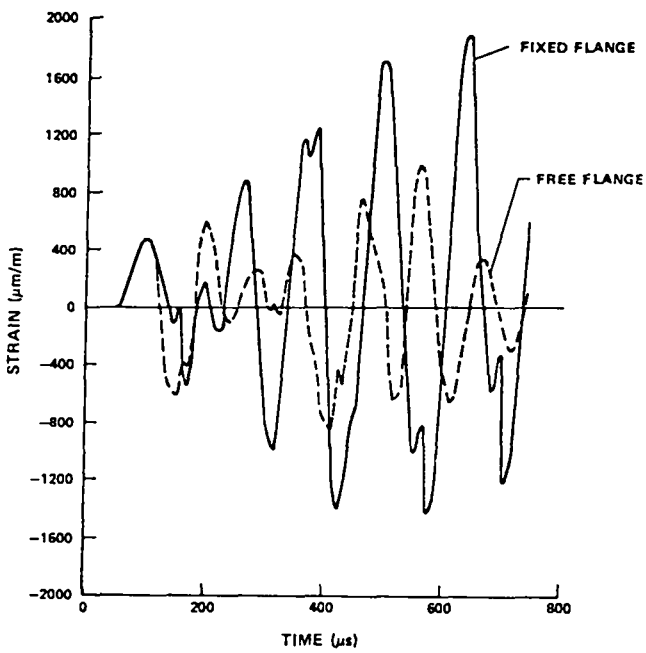

Fig. 20.
The calculated response of a test vessel for free- and fixed-flange boundary conditions (0.352-m-diam vessel with a 6.35-mm-thick wall, 25.4-mm-diam PBX-9404 charge). Strain is measured in an element near the axis of symmetry in the circumferential direction.

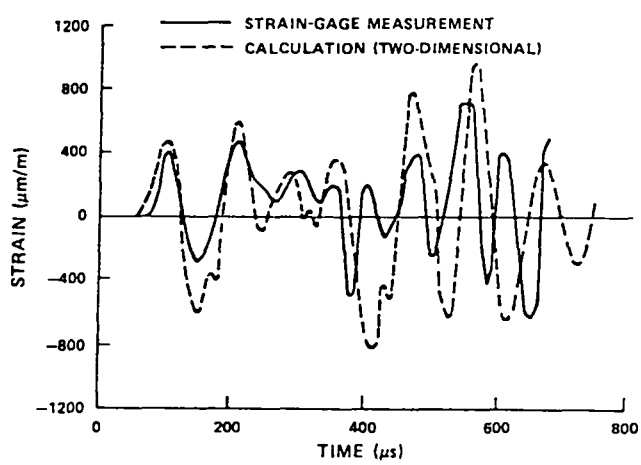

Fig. 21.
Comparison between calculated and measured strain in the vessel wall near the axis of symmetry (0.352-m-diam vessel with a 6.35-mm-thick wall, 25.4-mm-diam PBX-9404 charge).

was relatively low. A comparison between the fixed-flange calculation, Fig. 20, and the strain-gage measurement, Fig. 21, shows relatively poor agreement. Because the flange on the thin-wall vessel is relatively thin, we expect the free-flange calculations to agree with the experiment better than the fixed-flange calculations agree.

Figure 22 illustrates the results of an ADINA calculation for the thick-wall test vessel motion caused by the detonation of a 38.1-mm-diam explosive charge in an air-filled vessel. Shown are the initial configuration and the displaced configuration at 60, 130, and 200 μs after application of the loading pulse. The displacement has been multiplied by 200 to make the motion visible. The initial corner position of each element is indicated by a dot. At 60 μs, we see both the perfectly spherical motion of the vessel's upper portion and a wave propagating from the flange toward the vessel pole. After 130 μs, the motion is far from spherical, and there is significant bending motion in the vessel.

Figure 23 shows the agreement between measured and calculated strain at the strain-gage locations. The calculation was performed with the fixed-flange boundary condition. Because the thick-wall test vessel has a massive flange, the fixed-flange condition should represent the physical configuration somewhat better than the free-flange condition does. An elastic-plastic material model was used because the strains attain a fairly high level. The yield strength, which was used in the von Mises yield criterion, was taken as 207 MPa. A work hardening modulus of 20.7 GPa was used in the isotropic hardening model of ADINA. This value is 10% of Young's modulus. Agreement between calculated and measured strain is good. However, a phase shift occurs at about 500 μs; significant yielding occurs in the strain-gage area shortly before the phase shift.

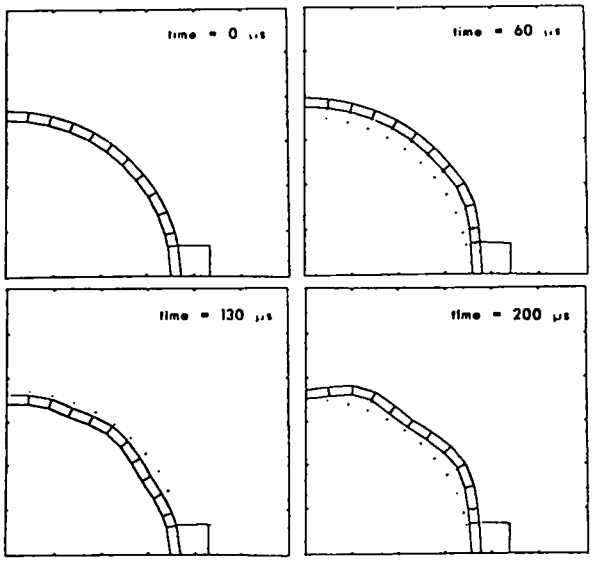

Fig. 22.
The displaced configuration of a test vessel, at selected times, as calculated by ADINA (0.352-m-diam vessel with a 10.6-mm-thick wall, 38.1-mm-diam PBX-9404/9501 charge). The displacement has been multiplied by 200.

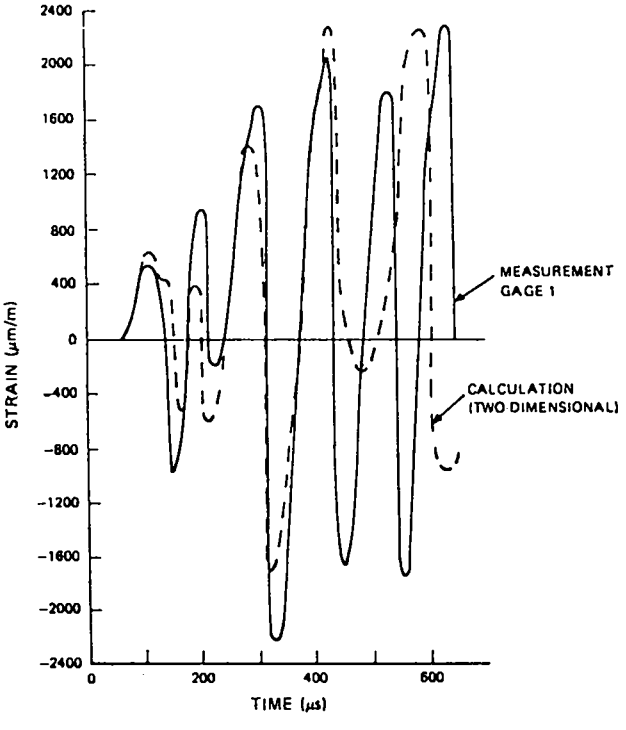

Fig. 23.
Comparison between calculated and measured strain in the vessel wall near the axis of symmetry (0.352-m-diam vessel with a 10.6-thick wall, 38.1-mm-diam PBX-9404/9501 charge).

V. EFFECT OF SURROUNDING MEDIA ON VESSEL REPONSE

When a spherical shell is surrounded externally by a medium of significant density, the motion of the shell couples with the motion of the surrounding material. In this section, we attempt to estimate the effect of this coupling by analyzing the response of a spherical shell embedded in a fluid medium and impulsively loaded. The shell's equation of motion is

$$\frac{d^2u}{dt^2} + \omega^2 u = \frac{P(t)}{\rho h} \quad , \tag{3}$$

where P(t) is now the net internal pressure acting on the shell, that is, the difference between the internal pressure, P_{IN}, and the external pressure, P_{EX},

$$P(t) = P_{IN} - P_{EX} \quad . \tag{22}$$

The surrounding medium, which is assumed to be infinite in extent, is governed, for an inviscid, compressible fluid, by the wave equation

$$\frac{1}{r^2}\left[\frac{\partial}{\partial r}\left(r^2 \frac{\partial \phi}{\partial r}\right)\right] = \frac{1}{c_f^2}\frac{\partial^2 \phi}{\partial t^2} \quad , \tag{23}$$

where r is the radial coordinate, c_f is the sound speed in the fluid, and ϕ is the velocity potential function, $\phi(r,t)$. The pressure, P, and particle velocity, v_f, within the fluid are expressed in terms of the velocity potential by

$$P = \rho_f \frac{\partial \phi}{\partial t} \quad , \quad v_f = -\frac{\partial \phi}{\partial r} \quad , \tag{24}$$

where ρ_f is the fluid density. The fluid and shell motion are coupled by requiring the pressure and particle velocity to be continuous across the fluid-shell interface. This boundary condition restricts the analysis to cases that do not result in cavitation. The pressure acting on the exterior of the shell is

$$P_{EX}(t) = \rho_f \left.\frac{\partial \phi}{\partial t}\right|_{r=R} \quad ,$$

where R is the average shell radius, and the shell velocity is set equal to the fluid velocity by the requirement

$$\frac{du}{dt} = -\left.\frac{\partial \phi}{\partial r}\right|_{r=R}$$

Initial conditions on the velocity potential function are taken as

$$\phi(r,o) = \frac{\partial \phi}{\partial r}(r,o) = \frac{\partial \phi}{\partial t}(r,o) = 0 \tag{25}$$

and on the shell as

$$u(0) = \frac{du}{dt}(o) = 0 \quad . \tag{26}$$

In addition, $\phi(r,t)$ must remain finite as $r \rightarrow \infty$.

For simplicity, consider the purely impulsive loading

$$P_{IN} = I_o \, \delta(t) \quad ,$$

where I_o is impulse per unit area and $\delta(t)$ is the Dirac Delta function. Note that the elastic vessel response for an arbitrary driving pressure-time history can be generated by suitable convolution of the impulsive solution. The exact solution to the above system of equations has been obtained, in Ref. 11, by using a transform technique. The resulting strain-time history in terms of non-dimensional variables can be expressed as

$$\varepsilon(\tau) = \bar{a} \, (1 - \nu) \, \bar{I} \left[\frac{(1/\eta-\alpha)e^{-\alpha\tau}}{(\beta-\alpha)\,(\gamma-\alpha)} + \frac{(1/\eta-\beta)e^{-\beta\tau}}{(\alpha-\beta)\,(\gamma-\beta)} \right.$$

$$\left. + \frac{(1/\eta-\gamma)e^{-\gamma\tau}}{(\alpha-\gamma)\,(\beta-\gamma)} \right] \quad , \tag{27}$$

where α, β, and γ are roots of the polynomial expression

$$S^3 - \frac{1}{\eta}(1 + \bar{a}\mu) \; S^2 + 2S - 2/\eta = 0$$

and the nondimensional parameters appearing in the above solution are defined by

$$c_s = \left[\frac{E}{\rho(1-\nu)} \right]^{1/2}$$

$$\mu = \rho_f/\rho$$

$$\bar{I} = \frac{I_o c_s}{ER}$$

$$\eta = c_s/c_f$$

$$\bar{a} = R/h$$

$$\tau = c_s t/R$$

Equation (27), which applies to spherically symmetric shell motion, was used to compute the maximum strain occurring in the shell as a function of each surrounding material that we considered. Table I lists the material properties, obtained from Ref. 12. The result was compared to the computed maximum strain that results if the surrounding medium is not present. Results of the calculations for a typical steel vessel with a radius-to-thickness ratio of 28 are given in Table II. The second column of Table II shows that the peak strain in this vessel can be reduced substantially by embedment in these materials. In particular, burial in concrete reduces peak strain nearly 70%.

Strength, cavitation, and reloading ("water hammer") effects are not considered in these results. Further, the results are based upon an infinite surrounding medium, that is, material extending sufficiently far that no signals return from boundaries during the vessel's significant response time. Obviously, some materials, particularly limestone, may not be practical from a fabrication standpoint.

Finally, the influence of the radius-to-thickness ration, R/h, for all surrounding media is indicated in Fig. 24. As the shell becomes thicker, reduction in strain becomes smaller, as expected because the more massive shell is influenced to a lesser degree by the surrounding medium. As the shell becomes thinner, the surrounding medium plays as ever-increasing role.

VIII. CONCLUSIONS

The sensitivity of the peak strain to the shape of the blast-wave pressure pulse has been investigated in a spherical vessel undergoing one-dimensional motion. As expected, the peak strain decreases rapidly when the pressure pulse is spread over a time longer than about a quarter period of the vessel's natural vibration. A scaling law relating maximum strain to explosive charge mass and other relevant parameters has been derived and has been shown to correlate experimental data. The law includes the effect of the initial air density in the vessel; however, the maximum strain increases only slowly with increasing air density. Based upon this scaling law, we conclude that, for a wide range of radius-to-thickness ratios, the volume of steel required to contain a specified explosive charge varies only slightly with the ratio. This slight variation is such that extremely thin wall, large-radius vessels make inefficient use of vessel material. However, in addition to stress analysis criteria based on blast containment, other design criteria, such as fracture mechanics, may control the vessel's configuration.

TABLE I

PROPERTIES OF SURROUNDING MEDIA

Material	Density (kg/m^3)	Sonic Velocity (km/s)
Water	1.0×10^3	1.49
Saturated sand	2.0×10^3	1.49
Concrete[a]	2.36×10^3	3.2
Saturated sandy silt[a]	2.09×10^3	1.92
Limestone[a]	2.36×10^3	5.18

[a]Bar velocity is used as sonic velocity.

TABLE II

PEAK STRAIN REDUCTION FOR A STEEL SHELL, R/h = 28

Surrounding Material	Peak Strain Ratio (Embedded Vessel/Free Vessel)
Water	0.682
Saturated sand	0.515
Concrete	0.313
Saturated sandy silt	0.445
Limestone	0.276

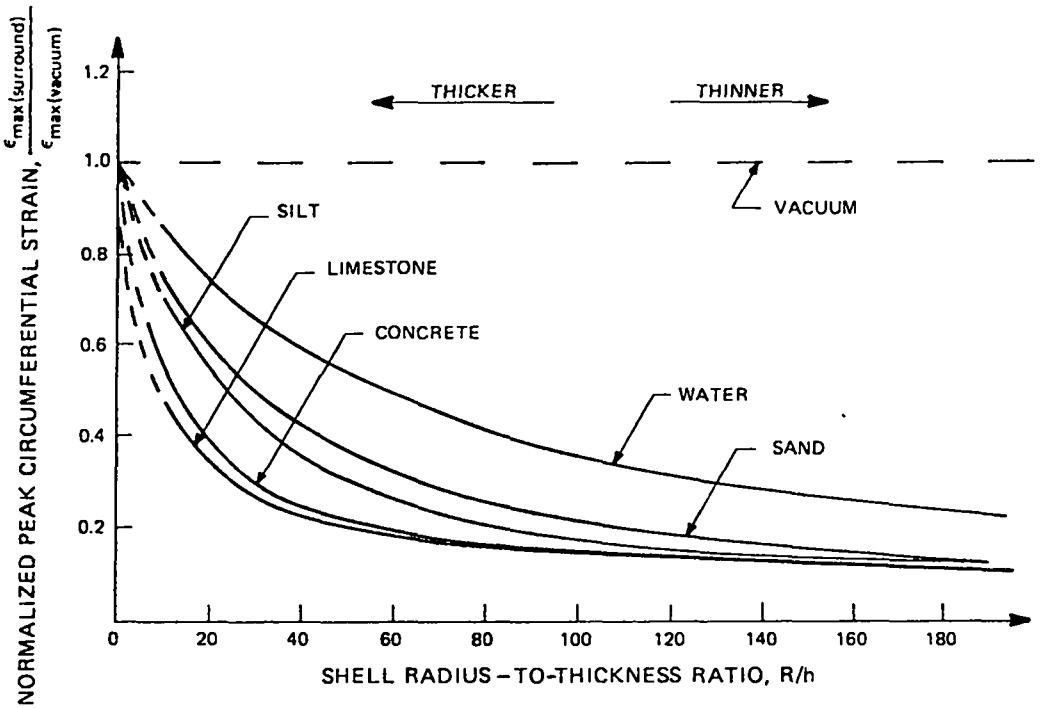

Fig. 24.
Peak strain reduction as a function of shell radius-to-thickness ratio for embedment in six materials.

Details of the blast-wave pressure pulse delivered to the vessel wall, analyzed with a one-dimensional, finite-difference code, show a fairly complex pulse structure. Calculated pressure loadings agree reasonably well with pressure gauge measurements. Vessel strain histories have been calculated with both one- and two-dimensional computer codes, and agreement between calculated results and strain-gage measurements is good. This result demonstrates the usefulness of these standard calculational techniques as design tools.

The effect of surrounding fluid media upon the response of impulsively loaded spherical vessels also has been estimated. A surrounding medium is most beneficial when the vessel has a large radius-to-thickness ratio.

The elastic response to explosive blast loading of containment vessels filled with air at arbitrary initial densities can be predicted with reasonable accuracy. Predictions can be based upon scaling-law fits to experimental data or, for greater detail, can be based upon finite-difference and finite-element computer code calculations. Future work will be directed toward a better understanding of the response of vessels containing compactable filler materials.

ACKNOWLEDGMENT

We acknowledge the support in the area of strain-gage instrumentation provided by the personnel of Group WX-10, especially Jack Thompson.

REFERENCES

1. R. H. Warnes, Los Alamos Scientific Laboratory, unpublished data, 1972, 1973, 1974, 1975.

2. T. R. Neal, Los Alamos Scientific Laboratory, unpublished data, January 1979.

3. W. E. Baker, P. S. Westine, and F. T. Dodge, *Similarity Methods in Engineering Dynamics, Theory and Practice of Scale Modeling* (Hayden Book Co., Inc., Rochelle Park, New Jersey, 1973), pp. 53-79.

4. R. W. Carlson, "Confinement of an Explosion by a Steel Vessel," Los Alamos Scientific Laboratory report LA-390 (September 1945).

5. W. Fickett, "PAD, A One-Dimensional Lagrangian Hydrocode," Los Alamos Scientific Laboratory report LA-5910-MS (April 1975).

6. G. I. Taylor, "The Dynamics of the Combustion Products Behind Plane and Spherical Detonation Fronts in Explosives," Proc. Roy. Soc. (London) A, **200**, 235 (1950).

7. E. L. Lee, H. C. Hornig, and J. W. Kury, "Adiabatic Expansion of High Explosive Detonation Products," Lawrence Livermore Laboratory report UCRL-50422 (May 1968).

8. H. L. Brode, "Blast Waves from a Spherical Charge," Phys. of Fluids **2**, 2, 217 (1959).

9. K. J. Bathe, "ADINA, A Finite Element Program for Automatic Dynamic Incremental Nonliner Analysis," Massachusetts Institute of Technology report 82448-1 (September 1975, revised May 1976).

10. F. App. and C. Snell, Los Alamos Scientific Laboratory, personal communication, July 13, 1978.

11. T. A. Duffey, "Transient Response of Viscoplastic and Viscoelastic Shells Submerged in Fluid Media," J. Appl. Mech. **98**, 1 (March 1976).

12. R. E. Crawford, C. J. Higgins, and E. H. Bultmann, "The Air Force Manual for Design and Analysis of Hardened Structures," Air Force Weapons Laboratory report AFWL-TR-102 (October 1974).

Printed in the United States of America. Available from
National Technical Information Service
US Department of Commerce
5285 Port Royal Road
Springfield, VA 22161

Microfiche $3.00

001-025	4.00	126-150	7.25	251-275	10.75	376-400	13.00	501-525	15.25
026-050	4.50	151-175	8.00	276-300	11.00	401-425	13.25	526-550	15.50
051-075	5.25	176-200	9.00	301-325	11.75	426-450	14.00	551-575	16.25
076-100	6.00	201-225	9.25	326-350	12.00	451-475	14.50	576-600	16.50
101-125	6.50	226-250	9.50	351-375	12.50	476-500	15.00	601-up	

Note: Add $2.50 for each additional 100-page increment from 601 pages up.